Supplementary information

Li-Site Defects Induce Formation of Li-Rich Impurity Phases: Implications for Charge Distribution and Performance of $LiNi_{0.5-x}M_xMn_{1.5}O_4$ Cathodes (M = Fe and Mg; x = 0.05–0.2)

Beth E. Murdock[1,2,3], Jiayi Cen[3,4], Alexander G. Squires[3,5], Seán R. Kavanagh[6], David O. Scanlon[3,5], Li Zhang[2,3] and Nuria Tapia-Ruiz[2,3]*

[1]Department of Chemistry, Lancaster University, Lancaster, LA1 4YB, UK

[2]Department of Chemistry, Molecular Sciences Research Hub, Imperial College London, W12 0BZ, UK.

[3]The Faraday Institution, Quad One, Harwell Science and Innovation Campus, Didcot, OX11 0RA, UK

[4]Department of Chemistry and Thomas Young Centre, University College London, WC1H 0AJ, UK

[5]School of Chemistry, University of Birmingham, Birmingham, B15 2TT, UK

[6]Department of Materials and Centre for Processable Electronics, Imperial College London, SW7 2AZ, UK

*Corresponding author: n.tapia-ruiz@imperial.ac.uk

Contents

Experimental Information

Experimental Methods

Synthesis

Previous reports show that the preparation of unsubstituted LNMO via oxalate co-precipitation methods produces large chamfered polyhedral particles which can promote Li^+ ion diffusion whilst reducing the surface area and minimising side reactions, thus leading to desirable electrochemical performance and high-tap density.[1–4] $LiNi_{0.5}Mn_{1.5}O_4$ (LNMO), $LiNi_{0.5-x}Fe_xMn_{1.5}O_4$ (FeX) and $LiNi_{0.5-x}Mg_xMn_{1.5}O_4$ (MgX) (x = 0.05, 0.1, 0.15 and 0.2) were, therefore, synthesised according to previous reports. As such, stoichiometric amounts of lithium acetate (Alfa Aesar, 99%), nickel acetate (Aldrich, 99%), manganese acetate (Aldrich, 99%) and either magnesium or iron nitrate (Alfa Aesar, 98%) were stirred in deionised water (1h), and precipitated with oxalic acid (Alfa Aesar, 98%). The molar ratio of oxalic acid:cation was 1:1. The solution was stirred for 2 h at room temperature and dried overnight in a water bath (50 °C) with continual stirring to produce a mixed-metal oxalate $[LiNi_{0.5-x}M_xMn_{1.5}]C_2O_4$.[1] The dried precipitate was heated at 500 °C for 6 h (heating and cooling rate of 10 °C min^{-1}) to decompose the precursors into a mixed-metal oxide, allowing the release of CO_2 prior to pellet formation. The resulting mixed-metal oxide was then pressed into pellets (5 tons cm^{-2}) before sintering at 900 °C for 24 h (heating and cooling rate of 10 °C min^{-1}) to produce the spinel materials.

Electrochemical characterisation

Electrodes were prepared by casting a mixture of 80% spinel, 10% Super-P (TOB New Energy) and 10% PVDF (Alfa Aesar) in *N*-methylpyrrolidone (NMP) (Acros Organics, 99.5%) onto Al foil (TOB New Energy, > 99.5%, thickness = 12 μm). The cast slurry was dried at 80 °C overnight, punched into 12 mm discs and dried under vacuum for a further 12 h at 120 °C (mass loading = 3–3.5 mg cm^{-2}). Spinel/Li half-cells (2032-type coin-cells, TOB New Energy) were constructed using a spinel working electrode, a Li counter/reference electrode (TOB New Energy, 99.9%, ∅ = 15.6 mm, thickness = 1 mm) and 1 M $LiPF_6$ in ethylene carbonate (EC)/dimethyl carbonate (DMC) (1:1, v/v) (Aldrich, battery grade) as electrolyte. Room temperature charge/discharge galvanostatic measurements were conducted on a multichannel battery cycler (Neware) in the voltage window 3.5–4.9 V at 1C (147 mAh g^{-1}).

Powder X-ray and neutron diffraction

X-ray powder diffraction data were collected for all samples on a lab-based Rigaku SmartLab diffractometer in Bragg-Brentano geometry, using a glass sample holder, between 2θ = 10–90 ° (0.1 ° min^{-1}). Time-of-flight powder neutron diffraction (ND-ToF) data were collected for

selected samples (x = 0, 0.1, 0.2, **Table S1**). Experiments were carried out at the ISIS spallation neutron and muon source on the General Materials (GEM) diffractometer.[5] For the experiments, powdered samples were packed in an MBraun glovebox under argon (H_2O and O_2 < 0.1 ppm) into cylindrical vanadium cans (⌀ = 6 mm, h = 5.5 cm). Data were collected over a wide Q-range (0.01–50 Å) across several banks, arranged at different angles to the detector. Data collection time of 8 h was used to provide a high signal-to-noise ratio at a high Q.

Combined Rietveld refinement of ND-ToF bank 3 (24–45 °), bank 4 (50–74 °) and lab XRD data were performed using GSAS software with the EXPGUI graphical interface for samples x = 0, 0.1 and 0.2, (**Table S1**).[6,7] Refined parameters included lattice parameter (*a*), octahedral (16d) and tetrahedral (8a) site occupancy, isotropic atomic displacement parameters (ADP) (U_{iso}), and oxygen *xyz* coordinates. Oxygen site occupancy was fixed to 1 and U_{iso} values of transition metal atoms were constrained to be equal. Backgrounds were fit using a Chebyshev polynomial function and peak shapes using a pseudo-Voight function. Estimated standard deviation (ESD) values of parameters related to peak intensity, which are generally accepted to be underestimated by a factor of ca. 3, were scaled accordingly.[8] The absorption correction parameter was refined to account for ^{6}Li absorption in the neutron data. This correction factor was refined separately for each bank, with the result being small and consistent between banks. Note that the inclusion of an absorption correction factor in the structural refinement may result in a systematic underestimation of the ADP values, as the absorption correction factor is derived from the product of *U* and the scale factor.[9] However, due to the nature of the study, which considers an internal comparison between samples in which all sample refinements are treated in the same manner, the comparison between samples still holds. The same is true for comparing ESD values between refinements. The relatively high χ^2 value reported herein is a result of long ND-ToF data collection times and the large resulting number of data points, in which extremely minor differences between experimental and calculated patterns can cause a significant increase in the χ^2 value. In this case, R-factors are more indicative of the goodness-of-fit obtained.

For all other samples (x = 0.05 and 0.15), Le Bail refinements were performed to determine lattice parameters and phase fractions. Backgrounds were fit using a Chebyshev polynomial function and peak shapes were fit using a pseudo-Voight function. U_{iso} values for all atoms were fixed to 0.005 Å^2 for all atoms, and site occupancies were fixed according to the stoichiometric formulation. The 16d octahedral sites were assumed for all substituents (i.e., Mg and Fe) during Le Bail refinements.

Mn^{x+} calculations (Figure S7)

The average Mn^{x+} oxidation state in each sample was estimated from electrochemical data and the stoichiometry that resulted from combined Rietveld refinement of X-ray and neutron diffraction data (**Tables S2**–**4**). The feasibility of the structural models, obtained through Rietveld refinements, was then determined by comparing Mn^{x+} estimations from both methods.

Electrochemical estimates of Mn^{3+} concentrations in LNMO, FeX and MgX (X = 0.1 and 0.2) were derived from the 4 V specific charge capacity region in the galvanostatic data (OCV–4.375 V, see **Figure 5**) through the following equations (**Equations S1**–**S2**):

$$Mn^{3+}(g) = \frac{4\ V\ region\ specific\ charge\ capacity}{Mn^{3/4+}\ theoretical\ specific\ capacity} \quad \text{(Eq. S1)}$$

$$wt\ \%\ Mn^{3+}(in\ LNMO) = \frac{Mn^{3+}(g)}{Electrode\ active\ mass\ \ (g)} \quad \text{(Eq. S2)}$$

Note that the initial charge capacity was chosen to eliminate any changes in [Mn^{3+}] that may arise during cycling. The remaining Mn^{4+} content was determined to be the difference between the total refined Mn content (ca. 1.5 mol) and the estimated moles of Mn^{3+}, as determined above. The average oxidation state was then calculated from the sum of products of the estimated molar quantities of Mn^{3+} and Mn^{4+} and their respective charges (**Equation S3**), as follows:

$$x\ in\ Mn^{x+} = \frac{4\ Mol\ (Mn^{4+}) + 3\ Mol\ (Mn^{3+})}{Mol\ (Mn_{total})} \quad \text{(Eq. S3)}$$

The average oxidation state of Mn^{x+} was also determined, through **Equation S4,** in which the sum of products of charge and refined moles of cations and anions must be equal to charge balance. Such calculations were performed while assuming a Ni^{2+} oxidation state.

$$1Mol(Li^{+}) + 2Mol(Ni^{2+}) + XMol(M^{+}) + 1Mol(Mn^{x+}) - 2Mol(O^{2-}) = 0 \quad \text{(Eq. S4)}$$

where the charge (X) for M (Mg^{2+} and Fe^{3+}) is 2 and 3, respectively.

Estimation of impurity phase fractions from Li deficiencies (Figure 11)

Assuming that all Li lost from the Li site precipitates to form a Li_2MO_3 impurity phase, as opposed to migrating to the 16d site, then the *spinel phase : impurity phase* mole ratio should be $Li_{1-y}Ni_{0.5}Mn_{1.5}O_4 : \frac{y}{2}Li_2MO_3$, where y = 1-$f_{Li.}$ The wt% of impurity per mol of $LiNi_{0.5-x}M_xMn_{1.5}O_4$ can then be calculated by **Equation S5**.

$$wt\%(Li_2MO_3) = \frac{\left(\frac{y}{2}\right)MW(Li_2MO_3)}{\left(\frac{y}{2}\right)MW(Li_2MO_3)+MW(LiNi_{0.5-x}M_xMn_{1.5}O_4)} \quad \text{(Eq. S5)}$$

List of Figures (experimental)

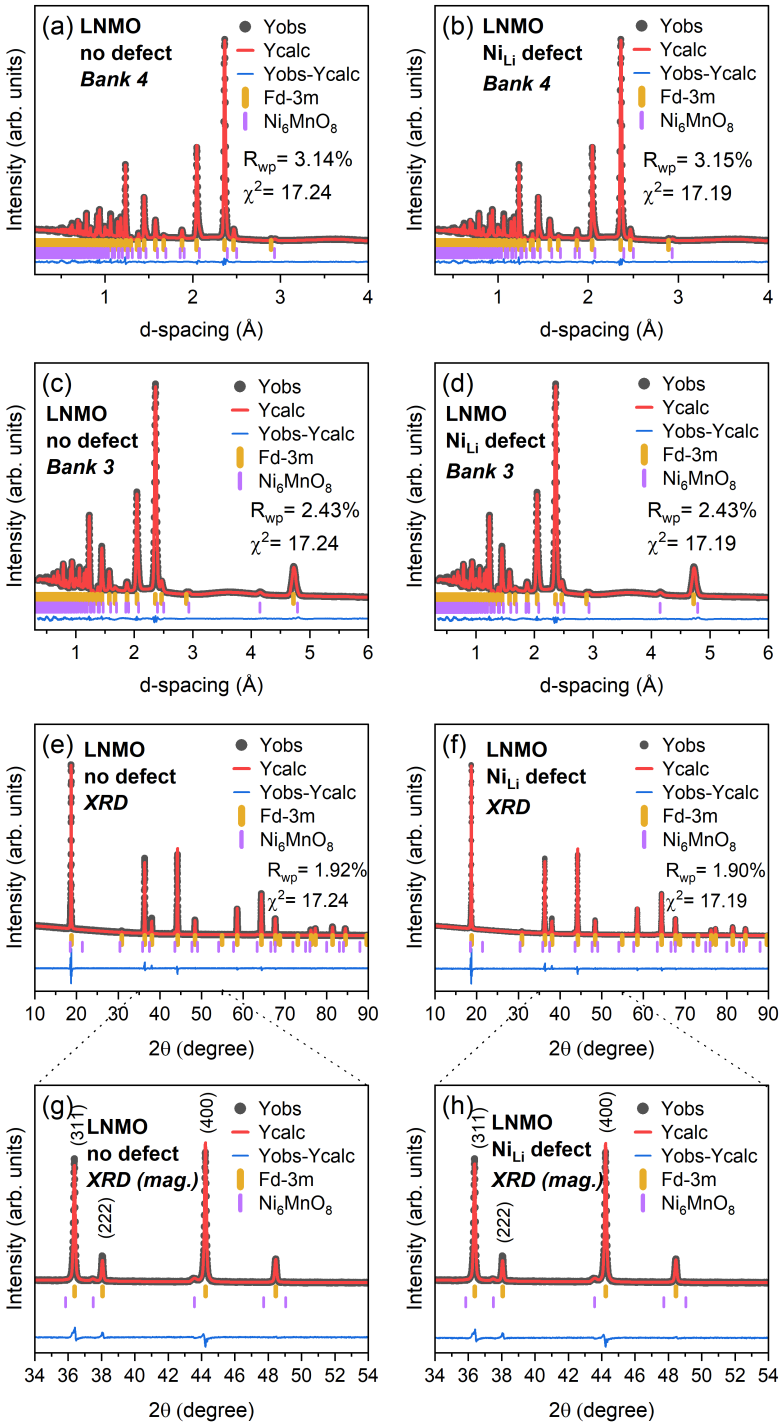

Figure S1. Combined XRD-ND Rietveld refinement against data collected at room temperature for LNMO. Structure models are based on the $Fd\bar{3}m$ space group and consider a Ni_6MnO_8 impurity and the following Li-site defects (A_{Li}): no defect (a, c, e and g); and Ni_{Li} defect (b, d, f and h). ND refinements of bank 4 (a–b) and bank 3 (c–d) show no change with defect scenario. XRD data (e–h) show a very subtle increase in the calculated (311) peak intensity when incorporating Ni_{Li} defects, as highlighted in the magnified plots (g–h).

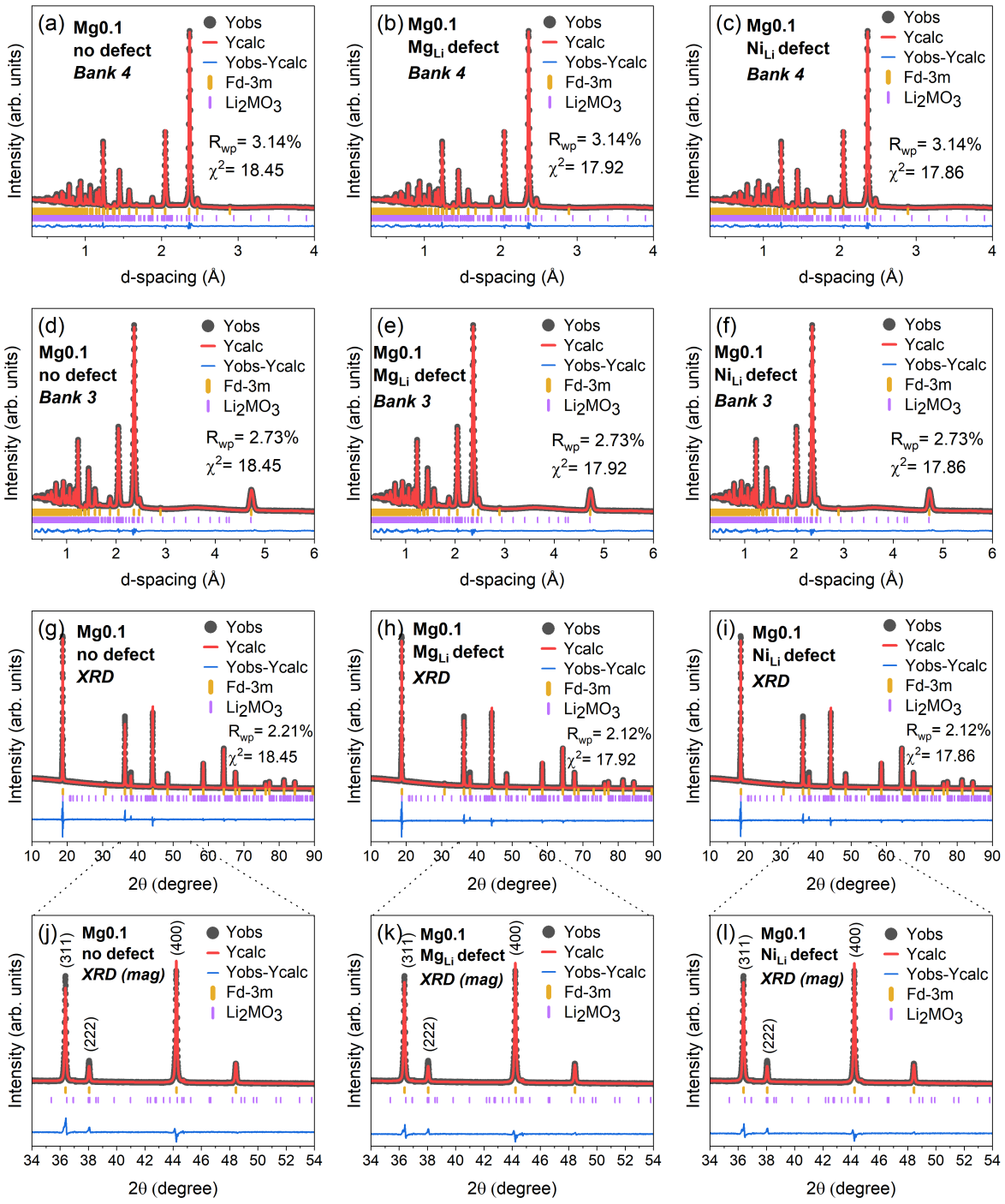

Figure S2. Combined XRD-ND Rietveld refinement against data collected at room temperature for Mg0.1. Structure models are based on the $Fd\bar{3}m$ space group and consider a Li_2MO_3 impurity (M = Mn and Ni) and the following Li-site defects (A_{Li}): no defect (a, d, g and j); Mg_{Li} defect (b, e, h and k); and Ni_{Li} defect (c, f, i and l). ND refinements of bank 4 (a–c) and bank 3 (d–f) show no change with defect scenario. XRD data (g–l) show an increase in the calculated (311) peak intensity when incorporating Mg_{Li}/Ni_{Li} defects, as highlighted in the magnified plots (j–l). Peak intensities, however, do not alter significantly between Ni_{Li} and Mg_{Li} scenarios (k–l).

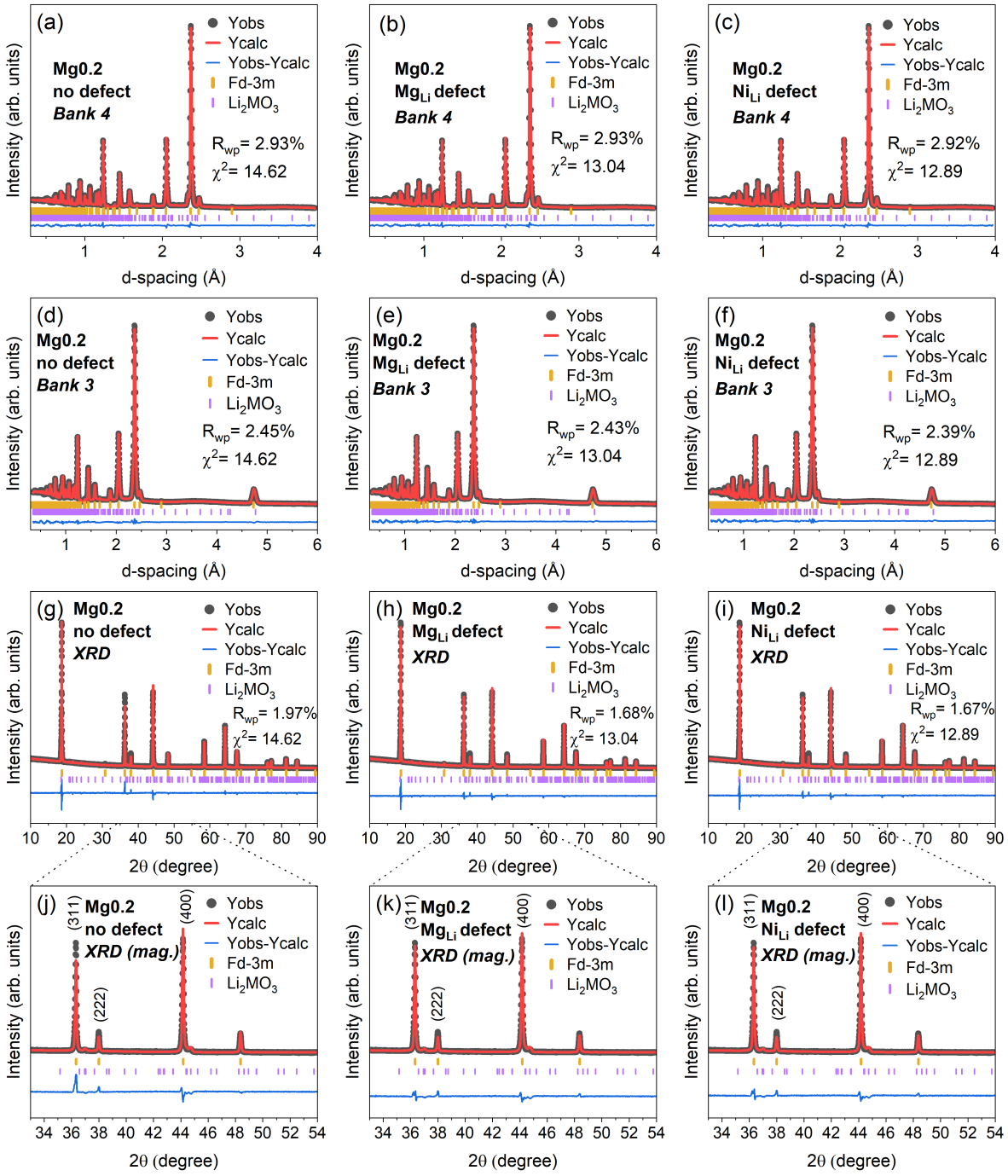

Figure S3. Combined XRD-ND Rietveld refinement against data collected at room temperature for Mg0.2. Structure models are based on the $Fd\bar{3}m$ space group and consider a Li_2MO_3 impurity (M = Mn and Ni) and the following Li-site defects (A_{Li}): no defect (a, d, g and j); Mg_{Li} defect (b, e, h and k); and Ni_{Li} defect (c, f, i and l). ND refinements of bank 4 (a–c) and bank 3 (d–f) show no change with defect scenario. XRD data (g–l) show an increase in the calculated (311) peak intensity when incorporating Mg_{Li}/Ni_{Li} defects, as highlighted in the magnified plots (j–l). Peak intensities, however, do not alter significantly between Ni_{Li} and Mg_{Li} scenarios (k–l).

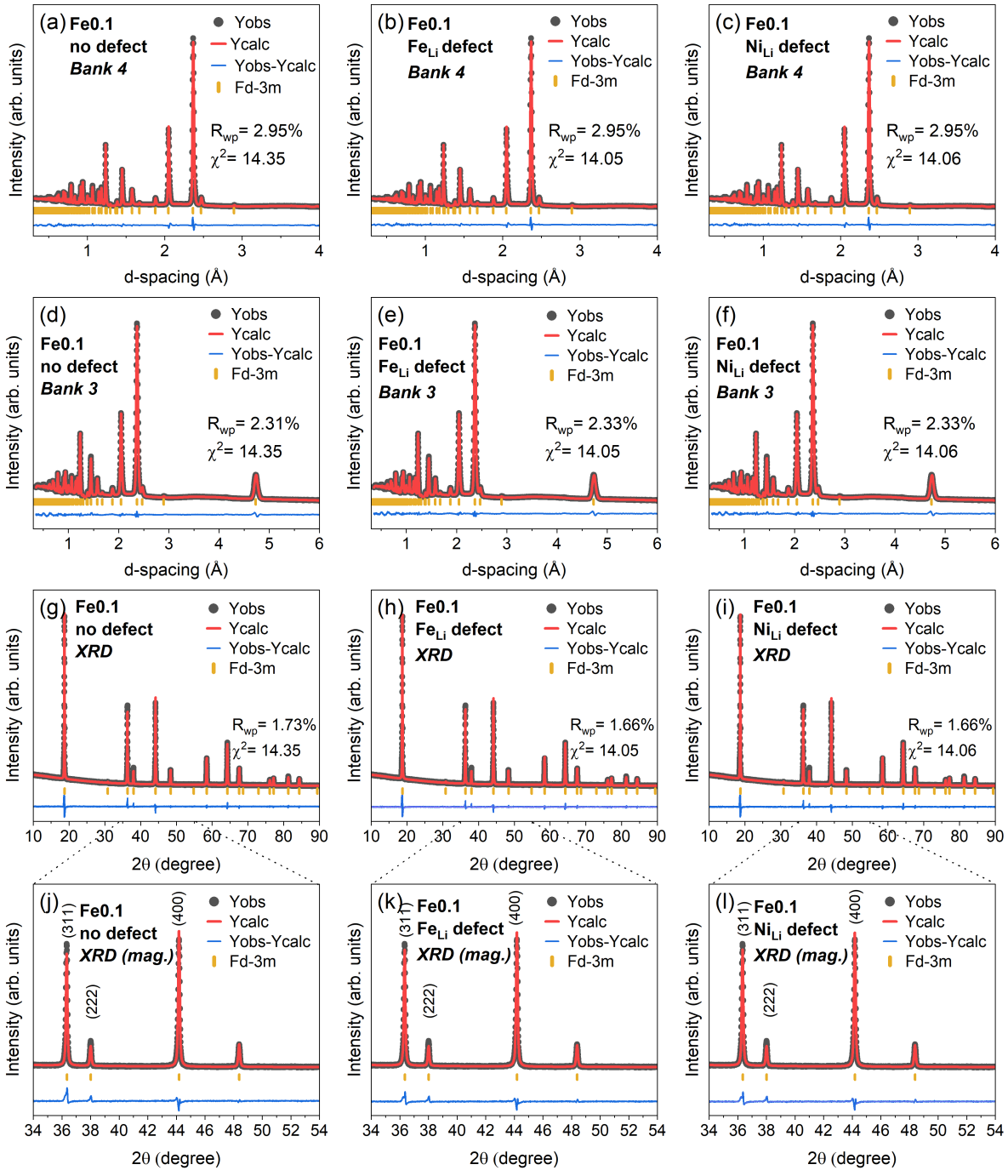

Figure S4. Combined XRD-ND Rietveld refinement against data collected at room temperature for Fe0.1. Structure models are based on the $Fd\bar{3}m$ space group and consider the following Li-site defects (A_{Li}): no defect (a, d, g and j); Fe_{Li} defect (b, e, h and k); and Ni_{Li} defect (c, f, i and l). ND refinements of bank 4 (a–c) and bank 3 (d–f) show no change with defect scenario. XRD data (g–l) show an increase in the calculated (311) peak intensity when incorporating Fe_{Li}/Ni_{Li} defects, as highlighted in the magnified plots (j–l). Peak intensities, however, do not alter significantly between Ni_{Li} and Fe_{Li} scenarios (k–l).

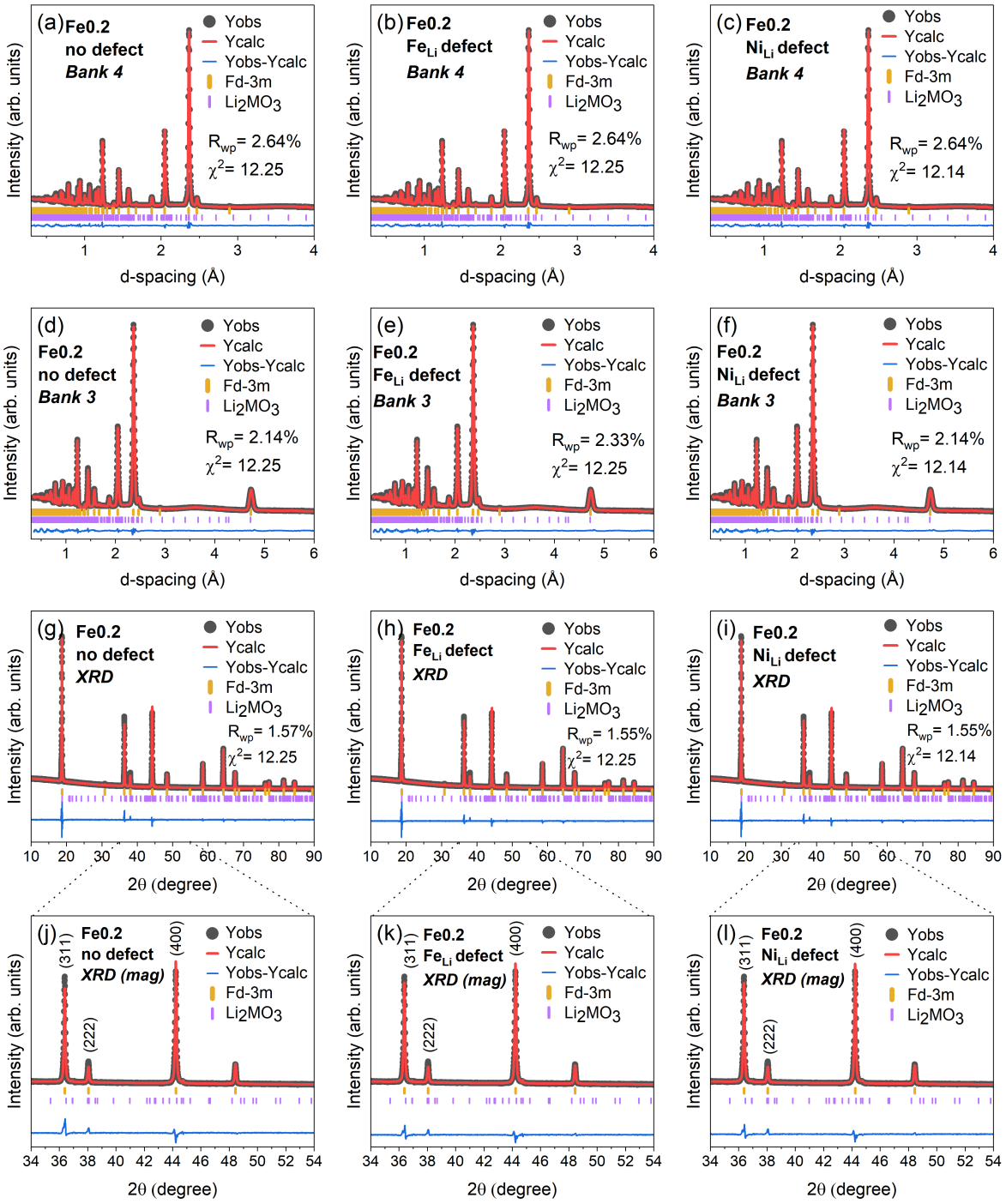

Figure S5. Combined XRD-ND Rietveld refinement against data collected at room temperature for Fe0.2. Structure models are based on the $Fd\bar{3}m$ space group and consider a Li_2MO_3 impurity (M = Mn and Ni) and the following Li-site defects (A_{Li}): no defect (a, d, g and j); Fe_{Li} defect (b, e, h, k); and Ni_{Li} defect (c, f, i and l). ND refinements of bank 4 (a–c) and bank 3 (d–f) show no change with defect scenario. XRD data (g–l) show an increase in the calculated (311) peak intensity when incorporating Fe_{Li}/Ni_{Li} defects, as highlighted in the magnified plots (j–l). Peak intensities, however, do not alter significantly between Ni_{Li} and Fe_{Li} scenarios (k–l).

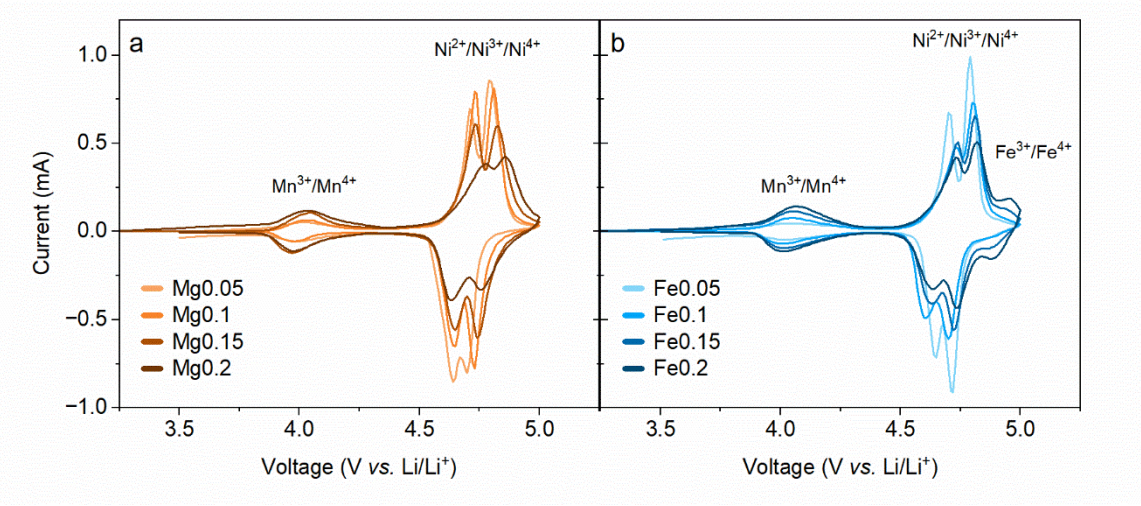

Figure S6. First cycle cyclic voltammograms of a) MgX and b) FeX (X = 0.05–0.2) collected in spinel/Li half-cells, using a voltage window of 3.5–5 V and a sweep rate of 0.1 mV s^{-1}. Note that a higher cut-off voltage was used in these measurements compared to the galvanostatic cycling data shown in the manuscript to identify the $Fe^{3+/4+}$ redox reaction and thus, illustrate the successful incorporation of Fe in the spinel substituted samples (b).

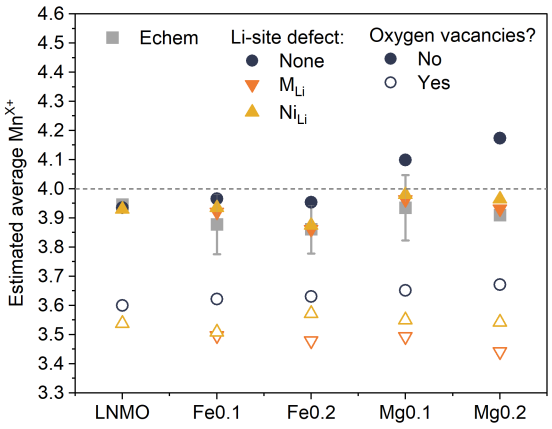

Figure S7. Estimated Mn^{x+} oxidation state from the 4 V specific charge capacity region in the galvanostatic data (OCV–4.375 V, Echem data) and Rietveld refinements (Li-site defects: None, M_{Li} and Ni_{Li}) both with (hollow) and without (filled) oxygen vacancies (V_o). The comparison between structural refinements and electrochemical data suggests that oxygen vacancies are overestimated within the refinement, resulting in overestimated Mn^{3+} concentrations. Due to such anticipated overestimation, refinements with oxygen vacancies

are discounted. Refinements in which $Mn^{x+} > Mn^{4+}$ are also discounted as they result from large, refined Li deficiencies (**Figure 3**).

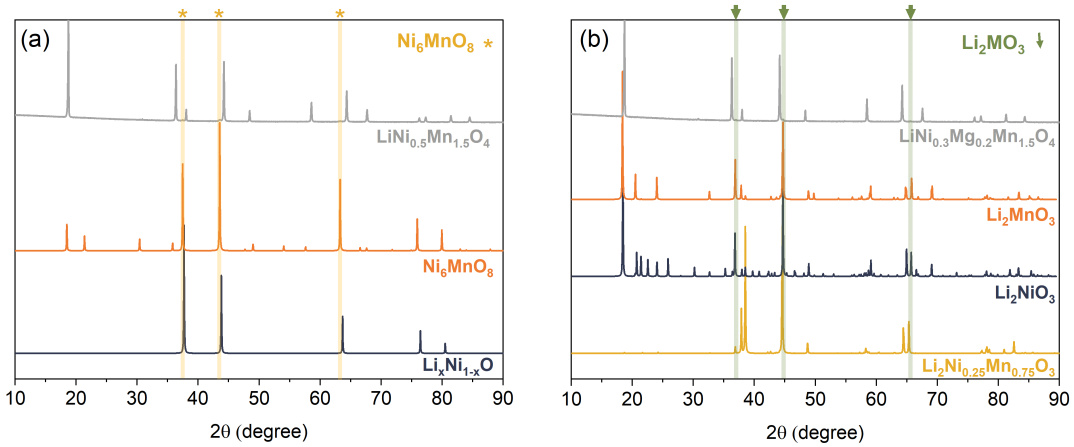

Figure S8. a) XRD data of as-synthesised LNMO compared against calculated patterns of typical Ni-rich impurity phases - Ni_6MnO_8 (ICSD #41890) and $Li_xNi_{1-x}O$ (ICSD #40584). The location of impurity peaks present in LNMO are highlighted using yellow asterisks. b) XRD data of Mg0.2 compared against Li_2MO_3-type impurity phases: Li_2MnO_3 (ICSD #132578), Li_2NiO_3 (ICSD #29337) and $Li_2Ni_{0.25}Mn_{0.75}O_3$ (ICSD #252826). Li_2MO_3 impurity peaks present in Mg0.2 are highlighted using green arrows.

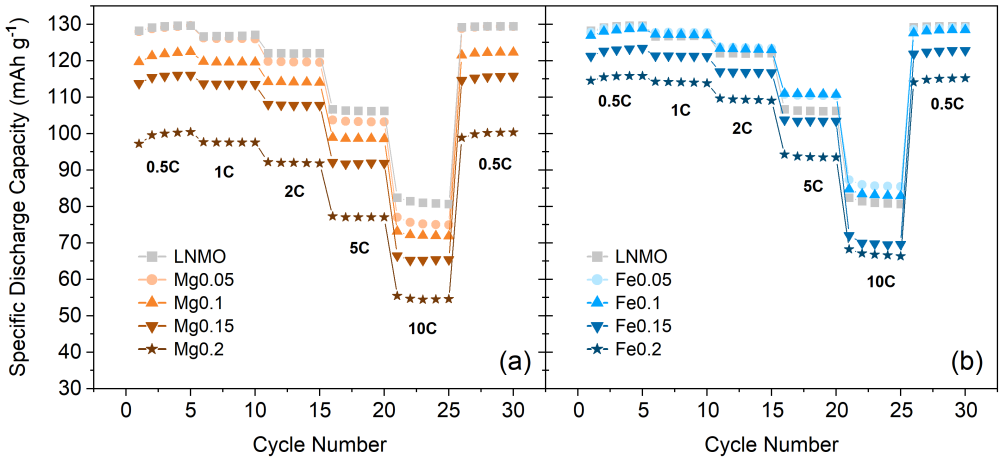

Figure S9. Rate capability of a) MgX and b) FeX (X = 0–0.2) collected in spinel/Li half-cells, using a voltage window of 3.5–4.9 V.

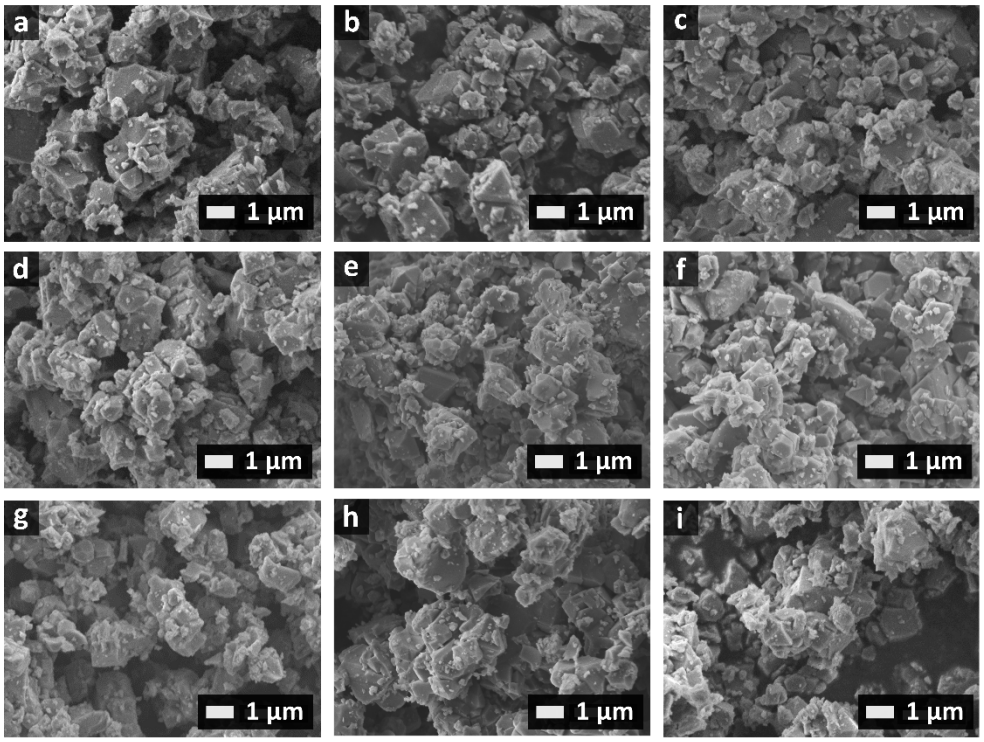

Figure S10. SEM images of a) Fe0.05; b) Fe0.1; c) Fe0.15; d) Fe0.2; e) Mg0.05; f) Mg0.1; g) Mg0.15; h) Mg0.2; and i) LNMO.

List of Tables (experimental)

Table S1. Summary of X-ray and neutron diffraction data collected for each sample.

	$LiNi_{0.5-x}Fe_xMn_{1.5}O_4$		$LiNi_{0.5-x}Mg_xMn_{1.5}O_4$	
x	*XRD*	*ND-ToF*	*XRD*	*ND-ToF*
0	✓	✓	✓	✓
0.05	✓	✗	✓	✗
0.1	✓	✓	✓	✓
0.15	✓	✗	✓	✗
0.2	✓	✓	✓	✓

Table S2. Crystallographic data obtained from Rietveld refinement against diffraction data on samples LNMO, Mg0.1, Mg0.2, Fe0.1 and Fe0.2 with no Li site defect. ESD values for refined parameters are provided in parentheses.

		Mg0.1	**Mg0.2**	**Fe0.1**	**Fe0.2**	**LNMO**
χ^2		18.45	14.62	14.35	12.25	17.24
R_{wp} %	ND-TOF bank 4	3.14	2.93	2.95	2.64	3.14
	ND-TOF bank 3	2.74	2.45	2.31	2.14	2.43
	XRD	2.21	1.97	1.73	1.57	1.92
$f_{(8a)}$	Li	0.849(24)	0.734(24)	0.972(21)	0.886(21)	1.000(24)
$f_{(16d)}$	Mn	0.760(1)	0.763(1)	0.760(1)	0.758(1)	0.775(1)
	Ni	0.190(1)	0.137(1)	0.190(1)	0.142(1)	0.225(1)
	M (M = Mg, Fe)	0.040(1)	0.087(1)	0.040(1)	0.092(1)	-
$f_{(32e)}$	O	1.000	1.000	1.000	1.000	1.000
*100*Uiso*	Li	1.945(104)	2.227(125)	1.908(82)	1.493(84)	1.576(76)
($Å^2$)	Ni, Mn, Mg/Fe	0.524(40)	0.395(33)	0.405(41)	0.592(35)	0.527(40)
	O	1.152(12)	1.195(12)	1.147(11)	1.172(11)	1.070(11)
xyz	8a	0.125000	0.125000	0.125000	0.125000	0.125000
	16d	0.500000	0.500000	0.500000	0.500000	0.500000
	32e	0.262996(18)	0.262991(17)	0.262952(18)	0.262999(17)	0.262931(18)
a (Å)		8.181623(59)	8.194190(56)	8.191654(59)	8.205752(64)	8.177138(57)

Table S3. Crystallographic data obtained from Rietveld refinement against diffraction data on samples LNMO, Mg0.1, Mg0.2, Fe0.1 and Fe0.2 in a Ni_{Li} defect scenario. ESD values for refined parameters are provided in parentheses.

		Mg0.1	**Mg0.2**	**Fe0.1**	**Fe0.2**	**LNMO**
χ^2		17.86	12.89	14.06	12.14	17.19
R_{wp} %	ND-TOF bank 4	3.14	2.92	2.95	2.64	3.15
	ND-TOF bank 3	2.73	2.39	2.33	2.14	2.43
	XRD	2.12	1.67	1.66	1.55	1.90
$f_{(8a)}$	Li	0.970(3)	0.947(3)	0.983(3)	0.979(3)	0.992(3)
	Ni	0.03(3)	0.053(3)	0.017(3)	0.021(3)	0.008(3)
$f_{(16d)}$	Mn	0.760(1)	0.763(1)	0.759(1)	0.758(1)	0.775(1)
	Ni	0.190(1)	0.137(1)	0.191(1)	0.141(1)	0.225(1)
	M (M = Mg, Fe)	0.040(1)	0.087(1)	0.041(1)	0.090(1)	-
$f_{(32e)}$	O	1.000	1.000	1.000	1.000	1.000
*100*Uiso*	Li	1.458(73)	1.235(65)	1.166(61)	1.475(60)	1.158(64)
($Å^2$)	Ni, Mn, Mg/Fe	0.653(40)	0.529(32)	0.440(40)	0.802(36)	0.534(39)
	O	1.144(12)	1.182(11)	1.135(11)	1.172(10)	1.070(11)
xyz	8a	0.125000	0.125000	0.125000	0.125000	0.125000
	16d	0.500000	0.500000	0.500000	0.500000	0.500000
	32e	0.263011(16)	0.263011(18)	0.262956(16)	0.263013(15)	0.262933(17)
a (Å)		8.181600(59)	8.194217(52)	8.191655(59)	8.205747(64)	8.177232(57)

Table S4. Crystallographic data obtained from Rietveld refinement against diffraction data on samples Mg0.1, Mg0.2, Fe0.1 and Fe0.2 in an M_{Li} defect scenario (M = Mg, Fe). ESD values for refined parameters are provided in parentheses.

		Mg0.1	**Mg0.2**	**Fe0.1**	**Fe0.2**
χ^2		17.92	12.95	14.05	12.25
R_{wp} %	ND-TOF bank 4	3.14	2.92	2.95	2.64
	ND-TOF bank 3	2.73	2.40	2.33	2.14
	XRD	2.12	1.68	1.66	1.55
$f_{(8a)}$	Li	0.947(6)	0.903(6)	0.981(3)	0.979(3)
	M (M=Mg, Fe)	0.053(6)	0.097(6)	0.019(3)	0.021(3)
$f_{(16d)}$	Mn	0.760(1)	0.763(1)	0.759(1)	0.758(1)
	Ni	0.190(1)	0.137(1)	0.191(1)	0.141(1)
	M (M=Mg, Fe)	0.04(1)	0.087(1)	0.041(1)	0.090(1)
$f_{(32e)}$	O	1.000	1.000	1.000	1.000
*100*Uiso*	Li	1.363(73)	1.275(89)	1.172(82)	1.528(61)
($Å^2$)	Ni, Mn, Mg/Fe	0.626(40)	0.484(32)	0.447(40)	0.792(36)
	O	1.143(12)	1.179(11)	1.133(11)	1.175(10)
xyz	8a	0.125000	0.125000	0.125000	0.125000
	16d	0.500000	0.500000	0.500000	0.500000
	32e	0.263008(18)	0.263018(16)	0.262957(16)	0.263016(15)
a(Å)		8.181611(59)	8.194218(53)	8.191655(59)	8.205749(64)

Computational information

Computational Methods

First-principles DFT calculations were performed using spin-polarised plane-wave DFT as implemented in the Vienna *ab initio* Simulation Package[10–12] (VASP) code (version 5.4.4). PAW pseudopotentials[13,14] (version PBE_5.4) of Li_*sv*, Mn_*pv*, Ni_*pv*, Fe_*pv*, Mg and O were used to model the core electrons. Calculations were performed with the GGA(PBEsol) + *U* method[15,16], where *U* values for *d*-orbitals of Mn, Ni and Fe were set to 3.9 eV, 6.0 eV and 4.0 eV, respectively, according to previous literature studies.[17,18] The initial primitive structure of *P*4$_3$32 LNMO obtained from Materials Project[19] contains 8 formula units of $LiNi_{0.5}Mn_{1.5}O_4$ (56 atoms). All calculations in this work used a plane-wave cut-off of 550 eV and defect calculations used a cubic 2×2×2 (448-atom) supercell with Γ-only **k**-point grid, consistent with our previous intrinsic defect study.[20] Tolerances of 10^{-5} eV and 10^{-2} eV Å^{-1} were applied to electronic and ionic convergence, respectively. The force tolerance was raised to 2×10^{-2} eV Å^{-1} for interstitial defects. Defect calculations were generated and analysed using the doped Python package.[21] A lean version of the ShakeNBreak[22] approach was used to aid the location of the ground-state defect structures.[23,24] Notably, the ground-state defect structure of Mg_{Li}^0 (with an Mn^{3+} formation near the defect site) was accessed by the ShakeNBreak approach, without considering standard defect structure relaxations. The ferrimagnetic spin configuration (Ni↓ Mn↑) was initialised for all defects with fixed-volume relaxations.[25]

The formation energy of a defect *X* in charge state *q* is defined as:

$$E^f(X^q) = E_{\mathrm{tot}}(X^q) - E_{\mathrm{tot}}(\mathrm{host}) - \sum_i n_i\mu_i + q(E_{\mathrm{vbm}} + \mu_{\mathrm{e}}) + \Delta^q, \qquad \text{(Eq. S6)}$$

where $E_{\mathrm{tot}}(X^q)$ and $E_{\mathrm{tot}}(\mathrm{host})$ are the total energies of a defect supercell and the defect-free (i.e., host) supercell respectively. μ_i is the atomic chemical potential of species i, and n_i is the number of atoms of species i that have been added (n_i > 0) or removed (n_i< 0) to form the defects. Sets of μ_i can be found by calculating the chemical potential limits of the host compound and they represent different experimental conditions.[26] μ_{e} is the electronic chemical potential (i.e., the Fermi level), referenced to the valence band maximum (VBM) of the host (E_{vbm}). Δ^q is a correction term to account for the finite-cell-size effect on the total energies of charged defects.[27,28] The Freysoldt, Neugebauer and Van de Walle[29,30] (FNV) charge correction scheme was used to be consistent with the previous intrinsic defect study.[20]

The defect formation energies should be evaluated at the equilibrium Fermi level which is determined self-consistently under the charge neutrality condition using py-sc-fermi:[31,32]

$$\sum_{X,q} qc(X^q) + n_h - n_e = 0 \qquad \text{(Eq. S7)}$$

where the net charge of a system takes into account all defect species (X) with charge q, free electrons (n_e) and free holes (n_h). The free carrier concentrations are determined according to the Fermi-Dirac distribution function.[33] The concentration c of a defect in thermodynamic equilibrium at temperature T is related to its formation energy E^f:[20,34]

$$c = N_{\text{sites}} N_{\text{config}} \exp\left(\frac{-E^f}{k_B T}\right) \quad \text{(Eq. S8)}$$

N_{sites} is the number of symmetry-inequivalent sites in the lattice per unit volume where the defect can be incorporated. N_{config} is the number of equivalent configurations (i.e., degeneracy) and k_B is the Boltzmann's constant. Defect concentrations for pristine, Mg- and Fe-substituted LNMO are given in **Table S5.**

Competing phases calculations

Potential impurity phases formed during the synthesis of LNMO can be predicted by evaluating the thermodynamic stability of the material by calculating all phases within the Li-Ni-Mn-O phase diagram. A small chemical potential stability window of LNMO with respect to the Ni chemical potential was predicted by a previous computational study.[20] Consequently, there is a small range of tolerable Ni-related conditions and deviation away from this would lead to Ni-rich impurity phase formation. The identities of impurity phases at each chemical potential limit (corresponding to a distinct preparation environment for LNMO) can be obtained provided that the structures of those phases are known. However, their quantities cannot be predicted.

Evaluating the thermodynamic stability of the doped systems requires calculating additional competing phases that can arise from the M dopant. The chemical potential limits for a quinary Li-M-Ni-Mn-O system are then automatically solved using the CPLAP code.[26] **Tables S10-11** show the chemical potential limits obtained for the Mg- and Fe-doped system arranged in order of increasing equilibrium Fermi levels, respectively. Each set of atomic chemical potentials corresponds to a distinct facet in the phase diagram where the named compounds are expected to exist in phase equilibria with the host compound. Both Ni_6MnO_8 and Li_2MnO_3 are predicted as impurity phases, but not the Li_2NiO_3 phase which conflicts with our previous suspicion of a greater likelihood of M = Ni for the Li_2MO_3 phase. Such discrepancy can be explained by the fact that our calculations assume a purely thermodynamic equilibrium process of materials synthesis which may not occur in practice. Additionally, given that the exact structures and compositions of $Li_xNi_{1-x}O$ are unknown, they are not captured by the calculations. It is possible that small quantities of impurity phases that account for the sources of Ni deficiency were formed.

List of Figures (computational)

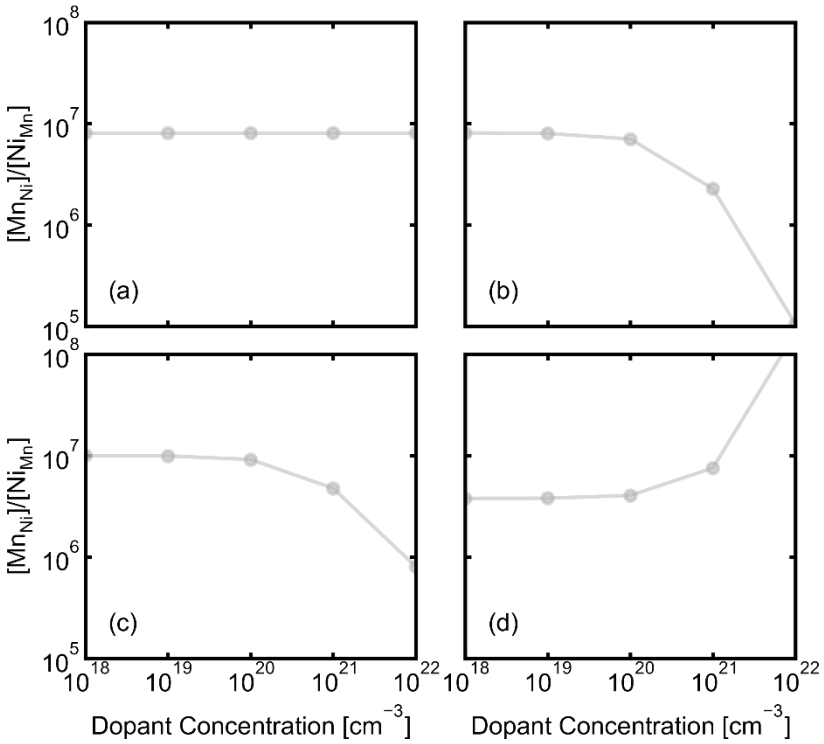

Figure S11. Calculated $[Mn_{Ni}]/[Ni_{Mn}]$ ratio in response to increased substituent concentration through tuning the concentration of extrinsic defect species Mg_{Ni} (a) and Mg_{Li} (b) in Mg-doped system and defect species Fe_{Ni} (c) and Fe_{Mn} (d) in Fe-doped systems, respectively.

List of Tables (computational)

Table S5. Calculated concentrations of relevant defect species at the chemical potential/growth conditions with the highest concentration of Mn^{3+} in pristine and Mg/Fe-doped LNMO. Defect concentrations are dependent on the growth conditions, thus the chosen chemical potential conditions allow comparison between the pristine and doped samples.

	Systems	Pristine	Mg-doped	Fe-doped
Concentration (cm^{-3})	Mn^{3+}	1.01×10^{18}	6.40×10^{20}	9.94×10^{20}
	Ni^{3+}	5.66×10^{3}	2.12×10^{17}	6.99×10^{16}
	Ni_{Mn}	5.95×10^{16}	8.93×10^{13}	1.57×10^{14}
	V_O	3.70×10^{15}	1.17×10^{10}	3.50×10^{11}
	V_{Ni}	8.96×10^{9}	1.21×10^{15}	4.07×10^{14}
	Mn_{Ni}	1.53×10^{19}	7.22×10^{20}	5.99×10^{20}
	Li_{Ni}	1.29×10^{19}	6.39×10^{20}	1.15×10^{21}
	Total X_{Ni}	2.82×10^{19}	1.36×10^{21}	1.75×10^{21}
	V_{Li}	3.94×10^{15}	9.84×10^{18}	1.99×10^{18}
	Mn_{Li}	3.79×10^{19}	2.94×10^{18}	5.00×10^{18}
	Ni_{Li}	4.50×10^{18}	1.21×10^{16}	9.09×10^{15}
	M_{Li}	0	5.06×10^{18}	2.26×10^{16}
	Total X_{Li}	4.24×10^{19}	1.79×10^{19}	7.02×10^{18}
	Total non-Li 8a occupancy	4.24×10^{19}	8.01×10^{18}	5.03×10^{18}

Table S6. Elemental phases calculated using the specified **k**-points in their standard states. Formation energies of elemental phases are zero by definition.

Species	Space group	**k**-points
Mg	$P6_3/mmc$	12 × 12 × 7
Fe	$Im\bar{3}m$	25 × 25 × 25
Li	$R\bar{3}m$	17 × 17 × 17
Mn	$I\bar{4}3m$	6 × 6 × 6
Ni	$Fm\bar{3}m$	21 × 21 × 21
O	$P\bar{1}$	1 × 1 × 1

Table S7. Formation energies of competing phases of LNMO ($Li_2NiMn_3O_8$) calculated with specified **k**-points. Space group detection used a tolerance of $1e^{-5}$.

System	Space group	**k**-points	Formation energy (eV atom^{-1})
$Li(NiO_2)_2$	$P4_32_12$	3 × 3 × 3	-1.43
$Li_2Mn_3NiO_8$	$P4_332$	3 × 3 × 3	-2.40
$Li_2Mn_3O_7$	$P\bar{1}$	5 × 4 × 4	-2.44
Li_2MnO_2	$P\bar{3}m1$	8 × 8 × 5	-2.38
Li_2MnO_3	$C2/m$	6 × 6 × 6	-2.42
Li_2Ni2O_3	$P\bar{1}$	8 × 5 × 3	-1.81
Li_2NiO_2	$P\bar{3}m1$	8 × 8 × 5	-1.84
Li_2NiO_3	$C2/m$	7 × 7 × 7	-1.64
Li_2O	$Fm\bar{3}m$	9 × 9 × 9	-1.89
Li_2O_2	$P6_3/mmc$	9 × 9 × 4	-1.49
Li_3MnO_4	$Pmn2_1$	5 × 5 × 4	-2.10
$Li_4Mn_2O_5$	$Pmm2$	7 × 2 × 7	-2.40
$Li_4Mn_5O_{12}$	$C2/c$	5 × 5 × 2	-2.45
$Li_5Mn_7O_{16}$	$Pnnm$	5 × 3 × 3	-2.50
Li_6MnO_4	$P4_2/nmc$	4 × 4 × 5	-2.11
$LiMn_2O_4$	$Pnma$	3 × 3 × 3	-2.59
$LiMnO_2$	$C2/m$	5 × 9 × 5	-2.61
$LiNiO_2$	$P2_1/c$	5 × 9 × 6	-1.68
$Mn(Ni_3O_4)_2$	$P1$	5 × 5 × 5	-1.89
Mn_2O_3	$Pbca$	3 × 3 × 3	-2.82
Mn_3O_4	$I4_1/amd$	4 × 4 × 3	-2.95
Mn_5O_8	$C2/m$	5 × 5 × 5	-2.74
MnNi	$Pm\bar{3}m$	13 × 13 × 13	-1.45
$MnNi_3$	$Pm\bar{3}m$	12 × 12 × 12	-0.76
$MnNiO_3$	$R\bar{3}$	6 × 6 × 6	-2.22
MnO	$I4/mmm$	6 × 6 × 6	-3.11
MnO_2	Pm	3 × 3 × 8	-2.42
Ni_3O_4	Pm	2 × 9 × 5	-1.41
NiO	$I4/mmm$	6 × 6 × 6	-1.71

Table S8. Formation energies of additional competing phases arising from Mg, calculated with specified **k**-points. Space group detection used a tolerance of $1e^{-5}$.

System	Space group	**k**-points	Formation energy (eV atom^{-1})
$Li_2MgMn_3O_8$	$P4_332$	$2 \times 2 \times 2$	-2.55
Mg_2Ni	$C222$	$6 \times 6 \times 3$	-0.13
Mg_6MnO_8	$I4/mmm$	$3 \times 3 \times 3$	-2.79
$MgMn_2O_4$	$I4_1/amd$	$4 \times 4 \times 3$	-2.85
$MgNi_2$	$P6_3/mmc$	$12 \times 12 \times 3$	-0.28
$MgNi_3$	$Pm\bar{3}m$	$8 \times 8 \times 8$	-0.08
MgO	$Fm\bar{3}m$	$6 \times 6 \times 6$	-2.82
MgO_2	$Pa\bar{3}$	$4 \times 4 \times 4$	-1.81

Table S9. Formation energies of additional competing phases arising from Fe, calculated with specified **k**-points. Space group detection used a tolerance of 1e-5.

System	Space group	**k**-points	Formation energy (eV atom^{-1})
$Fe(NiO_2)_2$	$I4_1/amd$	$3 \times 3 \times 3$	-1.65
$Fe_{13}O_{19}$	$C2/m$	$9 \times 9 \times 3$	-1.57
Fe_2NiO_4	$P4_322$	$2 \times 2 \times 2$	-1.86
Fe_2O_3	$P\bar{3}c1$	$4 \times 4 \times 1$	-1.82
Fe_3O_4	$P4_322$	$2 \times 2 \times 2$	-1.80
Fe_5O_7	$C2/m$	$10 \times 10 \times 3$	-1.69
FeNi	$P4/mmm$	$19 \times 19 \times 13$	-0.22
$FeNi_3$	$Pm\bar{3}m$	$13 \times 13 \times 13$	-0.20
FeO	$I4/mmm$	$7 \times 7 \times 5$	-1.66
FeO_2	$Pnma$	$7 \times 4 \times 2$	-1.34
Li_5FeO_4	$Pbca$	$2 \times 2 \times 2$	-1.95
$LiFe_5O_8$	$P4_332$	$2 \times 2 \times 2$	-1.92
$LiFeO_2$	$I4_1/amd$	$4 \times 4 \times 4$	-1.95
$Mn(FeO_2)_2$	$Fd\bar{3}m$	$2 \times 2 \times 2$	-2.26

Table S10. Chemical potential limits of the host LNMO, arranged in order of increasing self-consistent Fermi level, evaluated by considering all phases in the Li-Mg-Mn-Ni-O phase diagram.

Facet name	Fermi level (eV)	μ_{Li} (eV)	μ_{Mg} (eV)	μ_{Mn} (eV)	μ_{Ni} (eV)	μ_{O} (eV)
$Li_4Mn_5O_{12}$-$Li_2Mn_3NiO_8$-$Li_2MgMn_3O_8$-Li_2MnO_3-O_2	0.62	-3.51	-6.16	-7.50	-4.05	0.00
$Li_2Mn_3NiO_8$-Mg_6MnO_8-Li_2MnO_3-NiO-O_2	0.75	-3.35	-5.67	-7.81	-3.42	0.00
$Li_4Mn_5O_{12}$-$Li_2Mn_3NiO_8$-$Li_5Mn_7O_{16}$-$Li_2MgMn_3O_8$-O_2	0.81	-3.74	-6.25	-7.32	-4.14	0.00
$Li_4Mn_5O_{12}$-$Li_2Mn_3NiO_8$-$Li_5Mn_7O_{16}$-$Li_2MgMn_3O_8$-Li_2MnO_3	0.81	-3.37	-5.89	-6.95	-3.78	-0.27
$Li_2Mn_3NiO_8$-Mg_6MnO_8-$Li_2MgMn_3O_8$-Li_2MnO_3-O_2	0.81	-3.39	-5.68	-7.73	-3.57	0.00
$Mn(Ni_3O_4)_2$-$Li_2Mn_3NiO_8$-Mg_6MnO_8-NiO-O_2	0.83	-3.45	-5.68	-7.75	-3.42	0.00
MnO_2-$Li_2Mn_3NiO_8$-$Li_5Mn_7O_{16}$-$Li_2MgMn_3O_8$-O_2	0.87	-3.81	-6.26	-7.26	-4.15	0.00
$Mn(Ni_3O_4)_2$-$Li_2Mn_3NiO_8$-Mg_6MnO_8-$MnNiO_3$-O_2	0.94	-3.58	-5.70	-7.65	-3.44	0.00
MnO_2-$Li_2Mn_3NiO_8$-$Li_2MgMn_3O_8$-$MnNiO_3$-O_2	1.06	-3.97	-5.94	-7.26	-3.83	0.00
$Li_2Mn_3NiO_8$-Mg_6MnO_8-$Li_2MgMn_3O_8$-$MnNiO_3$-O_2	1.12	-3.75	-5.73	-7.48	-3.62	0.00
MnO_2-$Li_2Mn_3NiO_8$-$Li_5Mn_7O_{16}$-$Li_2MgMn_3O_8$-Mn_5O_8	1.14	-3.68	-5.86	-6.59	-3.75	-0.33
$LiMn_2O_4$-$Li_2Mn_3NiO_8$-$Li_5Mn_7O_{16}$-$Li_2MgMn_3O_8$-Mn_5O_8	1.23	-3.41	-5.50	-6.14	-3.38	-0.62
$LiMn_2O_4$-$Li_2Mn_3NiO_8$-$Li_5Mn_7O_{16}$-$Li_2MgMn_3O_8$-Li_2MnO_3	1.23	-3.02	-5.11	-5.75	-3.00	-0.91
MnO_2-$Li_2Mn_3NiO_8$-$Li_2MgMn_3O_8$-$MnNiO_3$-Mn_5O_8	1.23	-3.81	-5.61	-6.59	-3.50	-0.33
Mn_2O_3-$LiMn_2O_4$-$Li_2Mn_3NiO_8$-$Li_2MgMn_3O_8$-Mn_5O_8	1.24	-3.39	-5.46	-6.10	-3.35	-0.64
Mn_2O_3-$LiMn_2O_4$-$Li_2Mn_3NiO_8$-$Li_2MgMn_3O_8$-Mn_3O_4	1.37	-2.93	-4.77	-5.41	-2.66	-1.10
$LiMn_2O_4$-$Li_2Mn_3NiO_8$-$Li_2MgMn_3O_8$-Mn_3O_4-Li_2MnO_3	1.37	-2.85	-4.70	-5.34	-2.59	-1.16

Mn_2O_3-$MgMn_2O_4$-$Li_2Mn_3NiO_8$-$Li_2MgMn_3O_8$-Mn_3O_4	1.41	-2.97	-4.70	-5.41	-2.59	-1.10
$MgMn_2O_4$-$Li_2Mn_3NiO_8$-$Li_2MgMn_3O_8$-Mn_3O_4-Li_2MnO_3	1.41	-2.80	-4.54	-5.25	-2.43	-1.22
Mn_2O_3-$Li_2Mn_3NiO_8$-$Li_2MgMn_3O_8$-$MnNiO_3$-Mn_5O_8	1.43	-3.53	-5.18	-6.10	-3.07	-0.64
$MgMn_2O_4$-$Li_2Mn_3NiO_8$-Mg_6MnO_8-$Li_2MgMn_3O_8$-Li_2MnO_3	1.44	-2.78	-4.46	-5.28	-2.35	-1.22
Mn_2O_3-$MgMn_2O_4$-Li2Mn_3NiO_8-$Li_2MgMn_3O_8$-$MnNiO_3$	1.45	-3.49	-5.13	-6.05	-3.02	-0.68
$MgMn_2O_4$-$Li_2Mn_3NiO_8$-Mg_6MnO_8-$Li_2MgMn_3O_8$-$MnNiO_3$	1.50	-3.38	-4.97	-5.97	-2.86	-0.75
$MgMn_2O_4$-$Li_2Mn_3NiO_8$-Mg_6MnO_8-Li_2MnO_3-NiO	1.53	-2.67	-4.31	-5.08	-2.06	-1.36
$MgMn_2O_4$-$Li_2Mn_3NiO_8$-Mn_3O_4-Li_2MnO_3-NiO	1.54	-2.66	-4.31	-5.02	-2.03	-1.40
$Mn(Ni_3O_4)_2$-$MgMn_2O_4$-$Li_2Mn_3NiO_8$-Mg_6MnO_8-NiO	1.55	-2.82	-4.44	-5.25	-2.18	-1.25
$Mn(Ni_3O_4)_2$-$MgMn_2O_4$-$Li_2Mn_3NiO_8$-Mn_3O_4-NiO	1.56	-2.80	-4.44	-5.14	-2.12	-1.30
Mn_2O_3-$MgMn_2O_4$-$Li_2Mn_3NiO_8$-Mn_3O_4-$MnNiO_3$	1.56	-3.07	-4.70	-5.41	-2.38	-1.10
$Mn(Ni_3O_4)_2$-$MgMn_2O_4$-$Li_2Mn_3NiO_8$-Mg_6MnO_8-$MnNiO_3$	1.56	-3.04	-4.62	-5.50	-2.36	-1.08
$Mn(Ni_3O_4)_2$-$MgMn_2O_4$-$Li_2Mn_3NiO_8$-Mn_3O_4-$MnNiO_3$	1.57	-3.00	-4.62	-5.33	-2.27	-1.16

Table S11. Chemical potential limits of the host LNMO, arranged in order of increasing self-consistent Fermi level, evaluated by considering all phases in the Li-Fe-Mn-Ni-O phase diagram.

Facet name	Fermi Level (eV)	μ_{Li} (eV)	μ_{Fe} (eV)	μ_{Mn} (eV)	μ_{Ni} (eV)	μ_{O} (eV)
$Li_2Mn_3NiO_8$-Fe_2NiO_4-NiO-$Mn(Ni_3O_4)_2$-O_2	0.66	-3.45	-4.81	-7.75	-3.42	0.00
$Li_2Mn_3NiO_8$-Li_2MnO_3-Fe_2NiO_4-NiO-O_2	0.61	-3.35	-4.81	-7.81	-3.42	0.00
$MnNiO_3$-$Li_2Mn_3NiO_8$-Fe_2NiO_4-$Mn(Ni_3O_4)_2$-O_2	0.76	-3.58	-4.80	-7.65	-3.44	0.00
$Li_2Mn_3NiO_8$-Li_2MnO_3-Fe_2NiO_4-$LiFe_5O_8$-O_2	0.76	-3.42	-4.68	-7.68	-3.67	0.00
$Li_2Mn_3NiO_8$-$Li_4Mn_5O_{12}$-Li_2MnO_3-$LiFe_5O_8$-O_2	0.83	-3.51	-4.66	-7.50	-4.05	0.00
$Li_2Mn_3NiO_8$-$Li_4Mn_5O_{12}$-$LiFe_5O_8$-$Li_5Mn_7O_{16}$-O_2	0.97	-3.74	-4.62	-7.32	-4.14	0.00
MnO_2-$Li_2Mn_3NiO_8$-$LiFe_5O_8$-$Li_5Mn_7O_{16}$-O_2	1.01	-3.81	-4.60	-7.26	-4.15	0.00
MnO_2-$MnNi_{O3}$-$Li_2Mn_3NiO_8$-Fe_2NiO_4-O_2	1.01	-3.97	-4.60	-7.26	-3.83	0.00
MnO_2-$Li_2Mn_3NiO_8$-Fe_2NiO_4-$LiFe_5O_8$-O_2	1.05	-3.95	-4.57	-7.26	-3.88	0.00
$Li_2Mn_3NiO_8$-$Li_4Mn_5O_{12}$-Li_2MnO_3-$LiFe_5O_8$-$Li_5Mn_7O_{16}$	0.97	-3.37	-4.25	-6.95	-3.78	-0.27
MnO_2-$MnNiO_3$- $Li_2Mn_3NiO_8$-Mn_5O_8-Fe_2NiO_4	1.19	-3.81	-4.10	-6.59	-3.50	-0.33
MnO_2-$Li_2Mn_3NiO_8$-Mn_5O_8-$LiFe_5O_8$-$Li_5Mn_7O_{16}$	1.21	-3.68	-4.09	-6.59	-3.75	-0.33
MnO_2-$Li_2Mn_3NiO_8$-Mn_5O_8-Fe_2NiO_4-$LiFe_5O_8$	1.22	-3.78	-4.07	-6.59	-3.55	-0.33
Mn_2O_3-$MnNiO_3$-$Li_2Mn_3NiO_8$-Mn_5O_8-Fe_2NiO_4	1.32	-3.53	-3.70	-6.10	-3.07	-0.64
$LiMn_2O_4$-$Li_2Mn_3NiO_8$-Mn_5O_8-$LiFe_5O_8$-$Li_5Mn_7O_{16}$	1.28	-3.41	-3.69	-6.14	-3.38	-0.62
$LiMn_2O_4$-Mn_2O_3-$Li_2Mn_3NiO_8$-Mn_5O_8-$LiFe_5O_8$	1.28	-3.39	-3.66	-6.10	-3.35	-0.64
Mn_2O_3-$Li_2Mn_3NiO_8$-Mn_5O_8-Fe_2NiO_4-$LiFe_5O_8$	1.32	-3.48	-3.65	-6.10	-3.18	-0.64
$LiMn_2O_4$-$Li_2Mn_3NiO_8$-Li_2MnO_3-$LiFe_5O_8$-$Li_5Mn_7O_{16}$	1.28	-3.02	-3.30	-5.75	-3.00	-0.91

Mn_2O_3-Mn_3O_4-$MnNiO_3$-$Li_2Mn_3NiO_8$-Fe_2NiO_4	1.50	-3.07	-3.13	-5.41	-2.38	-1.10
Mn_3O_4-$MnNiO_3$-$Li_2Mn_3NiO_8$-Fe_2NiO_4-$Mn(Ni_3O_4)_2$	1.51	-3.00	-3.05	-5.33	-2.27	-1.16
$LiMn_2O_4$-Mn_2O_3-Mn_3O_4-$Li_2Mn_3NiO_8$-$LiFe_5O_8$	1.39	-2.93	-3.02	-5.41	-2.66	-1.10
Mn_2O_3-Mn_3O_4- $Li_2Mn_3NiO_8$-Fe_2NiO_4-$LiFe_5O_8$	1.40	-2.96	-3.01	-5.41	-2.61	-1.10
$LiMn_2O_4$-Mn_3O_4-$Li_2Mn_3NiO_8$-Li_2MnO_3-$LiFe_5O_8$	1.39	-2.85	-2.94	-5.34	-2.59	-1.16
Mn_3O_4-$Li_2Mn_3NiO_8$-Li_2MnO_3-Fe_2NiO_4-$LiFe_5O_8$	1.40	-2.81	-2.87	-5.27	-2.46	-1.21
Mn_3O_4-$Li_2Mn_3NiO_8$-Fe_2NiO_4-NiO-$Mn(Ni_3O_4)_2$	1.50	-2.80	-2.85	-5.14	-2.12	-1.30
Mn_3O_4-$Li_2Mn_3NiO_8$-Li_2MnO_3-Fe_2NiO_4-NiO	1.48	-2.66	-2.71	-5.02	-2.03	-1.40

References

1. Liu, D., Han, J., and Goodenough, J.B. (2010). Structure, morphology, and cathode performance of Li 1-x [Ni 0.5 Mn 1.5]O 4 prepared by coprecipitation with oxalic acid. J. Power Sources *195*, 2918–2923.

2. Liu, Z., Jiang, Y., Zeng, X., Xiao, G., Song, H., and Liao, S. (2014). Two-step oxalate approach for the preparation of high performance LiNi 0.5Mn1.5O4 cathode material with high voltage. J. Power Sources *247*, 437–443.

3. Liu, H., Zhu, G., Zhang, L., Qu, Q., Shen, M., and Zheng, H. (2015). Controllable synthesis of spinel lithium nickel manganese oxide cathode material with enhanced electrochemical performances through a modified oxalate co-precipitation method. J. Power Sources *274*, 1180–1187.

4. Xiao, Y., Xiang, W., Zhang, J., Zhu, Y., and Guo, X. (2016). Synthesis of spinel LiNi0.5Mn1.5O4 as advanced cathode via a modified oxalate co-precipitation method. Ionics (Kiel). *22*, 1361–1368.

5. Williams, W.G., Ibberson, R.M., Day, P., and Enderby, J.E. (1997). GEM - General Materials Diffractometer at ISIS. Phys. B Condens. Matter *241–243*, 234–236.

6. Larson, A.C., and Von Dreele, R.B. (2004). General Structure Analysis System (GSAS),. Los Alamos Natl. Lab. Rep. LAUR 86-748 *748*.

7. Toby, B.H. (2001). EXPGUI, a graphical user interface for GSAS. J. Appl. Crystallogr. *34*, 210–213.

8. Cockcroft, J.K. (2006). Estimated Standard Deviations. Powder Diffr. Web. http://pd.chem.ucl.ac.uk/pdnn/refine1/errors.htm.

9. Hewat, A.W. (1979). Absorption corrections for neutron diffraction. Acta Crystallogr. *35*, 248–250.

10. Kresse, G., and Hafner, J. (1993). Ab initio molecular dynamics for liquid metals. Phys. Rev. B *47*, 558–561.

11. Kresse, G., and Furthmüller, J. (1996). Efficiency of ab-initio total energy calculations for metals and semiconductors using a plane-wave basis set. Comput. Mater. Sci. *6*, 15–50.

12. Kresse, G., and Furthmüller, J. (1996). Efficient iterative schemes for ab initio total-

energy calculations using a plane-wave basis set. Phys. Rev. A *54*, 11169–11186.

13. Blöchl, P.E. (1994). Projector augmented-wave method. Phys. Rev. B *50*, 17953–17979.

14. Kresse, G., and Joubert, D. (1999). From ultrasoft pseudopotentials to the projector augmented-wave method. Phys. Rev. B - Condens. Matter Mater. Phys. *59*, 1758–1775.

15. Perdew, J.P., Ruzsinszky, A., Csonka, G.I., Vydrov, O.A., Scuseria, G.E., Constantin, L.A., Zhou, X., and Burke, K. (2008). Restoring the density-gradient expansion for exchange in solids and surfaces. Phys. Rev. Lett. *100*, 1–4.

16. Dudarev, S., and Botton, G. (1998). Electron-energy-loss spectra and the structural stability of nickel oxide: An LSDA+U study. Phys. Rev. B - Condens. Matter Mater. Phys. *57*, 1505–1509.

17. Hautier, G., Ong, S.P., Jain, A., Moore, C.J., and Ceder, G. (2012). Accuracy of density functional theory in predicting formation energies of ternary oxides from binary oxides and its implication on phase stability. Phys. Rev. B - Condens. Matter Mater. Phys. *85*.

18. Mueller, T., Hautier, G., Jain, A., and Ceder, G. (2011). Evaluation of tavorite-structured cathode materials for lithium-ion batteries using high-throughput computing. Chem. Mater. *23*, 3854–3862.

19. Jain, A., Ong, S.P., Hautier, G., Chen, W., Richards, W.D., Dacek, S., Cholia, S., Gunter, D., Skinner, D., Ceder, G., et al. (2013). Commentary: The materials project: A materials genome approach to accelerating materials innovation. APL Mater. *1*.

20. Cen, J., Zhu, B., Kavanagh, S.R., Squires, A.G., and Scanlon, D.O. (2023). Cation disorder dominates the defect chemistry of high-voltage LiMn1.5Ni0.5O4 (LMNO) spinel cathodes. J. Mater. Chem. A, 13353–13370.

21. Kavanagh, S.R., Squires, A.G., Nicolson, A., Mosquera-Lois, I., Ganose, A.M., Zhu, B., Brlec, K., Walsh, A., and Scanlon, D.O. (2024). doped: PythonToolkit for Robust and Repeatable Charged Defect Supercell Calculations. J. Open Source Softw. *9*, 6433.

22. Mosquera-Lois, I., Kavanagh, S.R., Walsh, A., and Scanlon, D.O. (2022). ShakeNBreak: Navigating the defect configurational landscape. J. Open Source Softw. *7*, 4817.

23. Mosquera-Lois, I., Kavanagh, S.R., Walsh, A., and Scanlon, D.O. (2023). Identifying the ground state structures of point defects in solids. npj Comput. Mater. *9*.

24. Mosquera-Lois, I., and Kavanagh, S.R. (2021). In search of hidden defects. Matter *4*, 2602–2605.

25. Van De Walle, C.G., and Neugebauer, J. (2004). First-principles calculations for defects and impurities: Applications to III-nitrides. J. Appl. Phys. *95*, 3851–3879.

26. Buckeridge, J., Scanlon, D.O., Walsh, A., and Catlow, C.R.A. (2014). Automated procedure to determine the thermodynamic stability of a material and the range of chemical potentials necessary for its formation relative to competing phases and compounds. Comput. Phys. Commun. *185*, 330–338.

27. Hoang, K., and Johannes, M. (2016). Defect Physics and Chemistry in Layered Mixed Transition Metal Oxide Cathode Materials: (Ni,Co,Mn) vs (Ni,Co,Al). Chem. Mater. *28*, 1325–1334.

28. Kim, S., Hood, S.N., Park, J.S., Whalley, L.D., and Walsh, A. (2020). Quick-start guide for first-principles modelling of point defects in crystalline materials. JPhys Energy *2*, 1–8.

29. Freysoldt, C., Neugebauer, J., and Van de Walle, C.G. (2011). Electrostatic interactions between charged defects in supercells. Phys. Status Solidi Basic Res. *248*, 1067–1076.

30. Freysoldt, C., Neugebauer, J., and Van De Walle, C.G. (2009). Fully Ab initio finite-size corrections for charged-defect supercell calculations. Phys. Rev. Lett. *102*, 1–4.

31. Squires, A.G., Scanlon, D.O., and Morgan, B.J. (2023). py-sc-fermi: self-consistent Fermi energies and defect concentrations from electronic structure calculations. J. Open Source Softw. *8*, 4962.

32. Buckeridge, J. (2019). Equilibrium point defect and charge carrier concentrations in a material determined through calculation of the self-consistent Fermi energy. Comput. Phys. Commun. *244*, 329–342.

33. Kittel, C., and Kroemer, H. (1998). Thermal Physics (American Association of Physics Teachers).

34. Mosquera-Lois, I., Kavanagh, S.R., Klarbring, J., Tolborg, K., and Walsh, A. (2023). Imperfections are not 0 K: free energy of point defects in crystals. Chem. Soc. Rev. *52*, 5812–5826.